

mmRTI: Radio Tomographic Imaging using Highly-Directional Millimeter-Wave Devices for Accurate and Robust Indoor Localization

Avishek Patra¹, Ljiljana Simić¹ and Marina Petrova²

¹Institute for Networked Systems, RWTH Aachen University, Aachen, Germany

²Dept. of Communication Systems, School of ICT, KTH Royal Institute of Technology, Stockholm, Sweden

Email: {avp, lsi}@inets.rwth-aachen.de, petrovam@kth.se

Abstract—As a device-free approach, **radio tomographic imaging (RTI)** is ideally suited for low-cost indoor localization in context-aware Internet-of-Things applications. However, the fundamental RTI algorithm relies on shadowing of the line of sight (LOS) links and therefore, conventional RTI implementations using 2.4 GHz sensing networks (*microRTI*) fail to accurately localize users in multipath-rich indoor environments. The localization accuracy is further degraded by external human movement that affects the signal propagation. In this paper, we propose *mmRTI*, a novel RTI approach based on a highly-directional, millimeter-wave sensing network, that aims to improve indoor localization by **utilizing the LOS-dominant nature of millimeter-wave signal propagation**. We experimentally evaluate *mmRTI*, operating at 60 GHz, with and without human movement around the sensing network, in two indoor environments, and compare its performance against the conventional *microRTI* approach. We observe that *mmRTI* achieves a 90%-ile localization error of 0.07 m-0.25 m, an improvement of 2.41 m-2.60 m compared to *microRTI*, while remaining unaffected by external human movement, which degrades the *microRTI* localization accuracy by up to 1.2 m.

I. INTRODUCTION

Over the last decade, **radio tomographic imaging (RTI)** [1] has emerged as an attractive *device-free* localization approach. For the fundamental shadow RTI algorithm, proposed in [1], a point-to-point *sensing network* of radio nodes is deployed around the area of interest (AoI) within which the user is to be localized. Upon entering the AoI, a user affects the signal propagation in the network, and thereby, changes the received signal strength (RSS) at the receiving nodes. With the underlying concept that the RSS change is due to the shadowing of line of sight (LOS) links between the nodes, the algorithm generates a spatial distribution image of the user to localize it in the AoI. As a device-free approach, RTI can contribute significantly towards implementing context-aware, non-commercial and low-cost smart home or healthcare applications, such as [2], [3], proposed under the umbrella of the Internet-of-Things (IoT).

The first experimental evaluation of the shadow RTI algorithm was conducted in [4] using a sensing network

of omnidirectional, 2.4 GHz nodes (i.e., the conventional approach, which we call *microRTI*) in a free-space-like outdoor scenario to demonstrate its localization accuracy. However, extensive experimental evaluations of *microRTI* in [5], [6] show that the localization accuracy is severely degraded indoors due to multipath effects. The evaluations in [5], [6] further revealed that co-channel interference and motion around the **2.4 GHz** network make the received signal noisy, thereby further degrading the localization accuracy. Several modifications to the fundamental shadow RTI algorithm, such as [7]–[9], have been proposed in the literature. While these algorithms report reducing multipath effects, they fail to overcome the co-channel traffic and external motion impacts. Additionally, these algorithms are too complex for low-cost deployments.

In this paper, we present *mmRTI*, a novel approach that employs **a highly-directional, millimeter-wave (mm-wave) sensing network** to improve shadow RTI algorithm based indoor localization. Wireless signals in the mm-wave frequencies inherently experience higher path and material losses [10], [11] compared to the sub-6 GHz microwave frequencies. Consequently, mm-wave transmissions are **dominated by LOS propagation**, with small contributions from first order reflections [12]. We aim to utilize this property of mm-wave signals to overcome the multipath problem. Additionally, we propose using **directional antennas** to not only filter out any mm-wave reflections, but also to isolate the nodes from the effects of external human movement and co-channel interference. Co-channel interference is unavoidable in omnidirectional networks, especially in the crowded 2.4 GHz band, due to transmission/reception from all directions. By contrast, co-channel interference in directional 60 GHz networks is likely to be virtually non-existent; given their narrow antenna beamwidths, 60 GHz links act as *pseudowired* connections [13]. Furthermore, given the short wavelength, mm-wave transceivers are expected to have dimensions in the mm range and to be mass produced at a very low cost [14]. Therefore, we argue that mm-wave

RTI networks are more attractive than microwave RTI networks in both practical and economic aspects. In our work, we demonstrate the superior localization accuracy and robustness of *mmRTI*, by systematically experimentally evaluating its performance against the conventional *microRTI* approach in different indoor environments, with and without external human movement.

We note that *mmRTI* aims to improve indoor localization by altering the conventional *network* configuration only, without introducing any algorithmic changes. By contrast, several works in the literature have proposed modifying the underlying shadow RTI *algorithm* [1], [4] to mitigate the multipath effects. In [7], the authors consider multi-channel RSS changes to mitigate small scale fading effects. In [8], the fade level change is considered to adaptively determine a LOS link model. Short-term RSS variance is considered in [9] instead of instantaneous RSS changes. While these works report mitigation of multipath effects using 2.4 GHz omnidirectional nodes, the experiments were conducted in the absence of co-channel interference and external human motion. Additionally, these solutions are too complex for low-cost deployments: whereas [7] requires expensive multi-channel radios, it is challenging in practice to precisely compute fade levels for [8]. Furthermore, these solutions are not robust across different indoor scenarios: for example, [8] performs *worse* compared to the shadow RTI algorithm for experiments in [5], [6].

Our experimental results show that *mmRTI* greatly improves the indoor localization accuracy, both with and without external human motion. For example, without external motion, *mmRTI* achieves a 90%-ile localization error of 0.07 m in our conference hall scenario, compared to a 90%-ile error of 2.48 m obtained by *microRTI*. We also present *mmRTI* latency and AoI coverage studies to show the practical feasibility of *mmRTI* deployments.

The rest of the paper is structured as follows. In Section II we describe the fundamental shadow RTI algorithm. We present the proposed *mmRTI* approach in Section III. In Sections IV and V we present our experimental evaluation methodology and results. We conclude our work in Section VI.

II. SHADOW RTI ALGORITHM

In this section, we present the shadow RTI algorithm as proposed in [1], [4]. In an RTI sensing network of N nodes, there exist a total of $L = N(N - 1)$ links. In an environment with predominantly LOS links, an object on or near a link l causes the link RSS to change. The RSS change is measured by comparing the instantaneous RSS with the mean, empty-state RSS of a link. In other words, the RSS change results from the attenuation experienced by a link across the AoI. To discretely represent the link attenuation, the AoI is divided into $|\mathbf{M}|$ pixels of length d such that the attenuation for the entire AoI can be represented as an attenuation image vector \mathbf{x} (x^i is

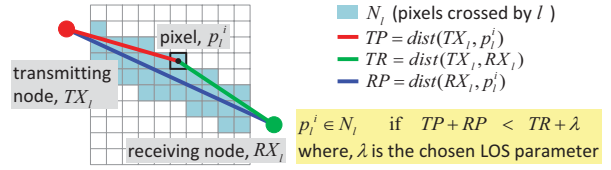


Fig. 1: Non-zero weighted pixel selection process for a link, l .

the attenuation across a pixel $p^i \in \mathbf{M}$). Accordingly, the RSS change for a link l can be represented as the sum of the attenuation experienced by the signal across each pixel crossed by the link. As shown in Fig. 1, the pixels \mathbf{N}_l crossed by a link l are selected based on the distance between the two nodes and the pixels. Therefore, the total attenuation of a link l can be represented in terms of \mathbf{x} and a weighting vector for the link, \mathbf{w}_l , as

$$S_l = \mathbf{w}_l^T \mathbf{x}, \quad (1)$$

such that all the pixels in \mathbf{N}_l have a weight equaling the inverse square root of the distance between the two nodes of the link, whereas the pixels in $\mathbf{M} - \mathbf{N}_l$ have a weight of 0. Considering all L links, the measured RSS change vector, \mathbf{y} , of the network can be represented as

$$\mathbf{y} = \mathbf{W} \mathbf{x} + \mathbf{n}, \quad (2)$$

where $\mathbf{W} = [\mathbf{w}_1, \dots, \mathbf{w}_L]^T$ is the weight vector matrix, and $\mathbf{n} = [n_1, \dots, n_L]^T$ is the measurement noise vector.

A relationship between the known \mathbf{y} and the unknown \mathbf{x} is established in (2). Since the measurements are superimposed with noise, it is desirable to find an approximate solution, $\hat{\mathbf{x}}$, in a least squares sense such that

$$\hat{\mathbf{x}} = \underset{\mathbf{x}}{\text{argmin}} \|\mathbf{W} \mathbf{x} - \mathbf{y}\|_2^2. \quad (3)$$

RTI estimation is an ill-posed inverse problem as typically, $L \ll |\mathbf{M}|$ and consequently, small measurement noise can make the image unstable. Therefore, a regularization technique [4] is applied to stabilize the image. In case of the Tikhonov Regularization, $\hat{\mathbf{x}}$ is determined by adding a weighted smoothing norm to (3), resulting in a damped least squares formulation as below

$$\hat{\mathbf{x}} = \underset{\mathbf{x}}{\text{argmin}} \|\mathbf{W} \mathbf{x} - \mathbf{y}\|_2^2 + \alpha \|\mathbf{D} \mathbf{x}\|_2^2, \quad (4)$$

where \mathbf{D} is the regularization matrix, chosen to impose desired properties to the image, and α is the regularization parameter. The least square problem is solved as

$$\hat{\mathbf{x}} = (\mathbf{W}^T \mathbf{W} + \alpha \mathbf{D}^T \mathbf{D})^{-1} \mathbf{W}^T \mathbf{y} = \mathbf{P} \mathbf{y}, \quad (5)$$

where \mathbf{P} is the projection matrix that is dependent on \mathbf{D} , α and \mathbf{W} . Once computed, \mathbf{P} remains constant, while \mathbf{y} varies with changes in the object position.

III. PROPOSED *mmRTI* APPROACH

For localization using *mmRTI*, a sensing network of directional 60 GHz nodes is deployed. Before localizing, the mean RSS measurement for an empty AoI is obtained

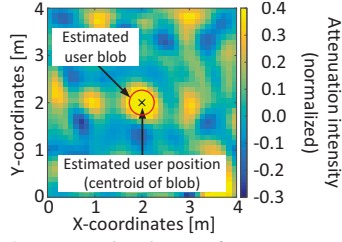


Fig. 2: Example attenuation image for a target user in the AoI, along with the selected blob and the estimated user position.

for each network link. When a target user enters the AoI, the instantaneous RSS for all the network links is measured. The RSS changes, computed with respect to the *empty-AoI* RSS, are then processed via the shadow RTI algorithm in Section II to generate an attenuation image, as in Fig. 2. From the attenuation image, the user *blob* (i.e., a contiguous set of pixels that have a difference higher than a selected threshold) is identified, from which the user location is estimated by computing the centroid of the blob. If there are multiple blobs in an attenuation image, the blob with the highest cumulative difference is selected for estimation.

While both *mmRTI* and *microRTI* adopt the shadow RTI algorithm to estimate the user location, there is a significant difference in their **network configuration** that greatly alters their RSS measurement procedures. When one omnidirectional node broadcasts in *microRTI*, all other sensing network nodes receive the signal. By contrast, *mmRTI* requires directional scanning, as only one directional node at a time receives the transmission from another directional node. Given that the RSS measurement latency, and thereby the localization accuracy of a mobile target, is dependent on the RSS measurements procedure, we present an analysis of the *mmRTI* and *microRTI* RSS measurement latency for different network sizes in Section III-A. Additionally, due to the narrow antenna beamwidths, an *mmRTI* node covers only a fraction of the AoI for an instantaneous antenna orientation, compared to an omnidirectional *microRTI* node. We thus present in Section III-B a relation between the number of network nodes and the AoI size to ensure complete AoI coverage, and thereby, the detectability of a target user with *mmRTI*.

A. Latency Comparison

The RSS measurement latency for a complete sensing network depends on the number of transmission rounds, the transmission duration per round and the channel access delay. For our analysis, we assume the same transmission duration per round for both the networks. Considering the difference in their RSS measurement procedures, the number of transmission rounds required to measure the complete network RSS in *microRTI* and *mmRTI* equals the number of network nodes, N , and network links, $L = N(N - 1)$, respectively (assuming one node transmitting per round). Accordingly, for

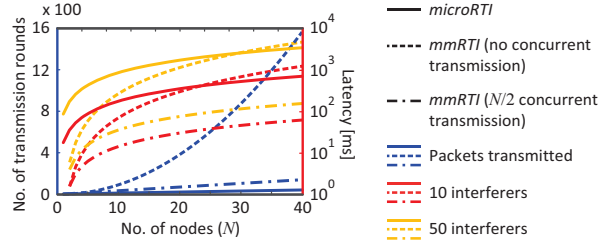


Fig. 3: Number of transmission rounds (blue) and network RSS measurement latency (red and yellow) for *microRTI* and *mmRTI* sensing networks of different sizes.

collision-free channel access, the RSS measurements will be updated faster for *microRTI*, which is crucial for accurate localization of a mobile target. However, given the widespread deployment of 2.4 GHz networks, we cannot expect collision-free access in practice. The average IEEE 802.11 DCF MAC access delay for 2.4 GHz omnidirectional WLANs is 8 ms–88 ms for 5–50 interferers [15]. By contrast, co-channel interference is largely non-existent in 60 GHz networks as the directional links behave as *pseudowired* connections [13]. Accordingly, the access delay in 60 GHz networks is significantly lower. In [16], the average IEEE 802.11ad hybrid CSMA/CA-based MAC access delay for a 60 GHz network is estimated to be 0.8 ms–3 ms for 5–50 interferers.

In Fig. 3, we present the RSS measurement latencies for *microRTI* and *mmRTI*, considering the average access delays for 10 and 50 interferers. From Fig. 3, we observe that given the higher access delay in 2.4 GHz networks, the RSS measurement latency in *mmRTI* is lower than *microRTI* for up to a 22-node and a 30-node network, considering 10 and 50 interferers, respectively. Therefore, even though *mmRTI* requires more transmission rounds, the latency is nonetheless lower than *microRTI* for *practical* network sizes. Furthermore, we note that the *mmRTI* latency can be further reduced by scheduling concurrent transmissions over multiple, non-interfering directional links in one round. Although such scheduling depend on the network geometry and the deployment scenario, from Fig. 3, we observe that for the best case scenario of $N/2$ concurrent, non-interfering transmissions per round (at a given instant, a maximum of $N/2$ directional links are possible in a N -node network), the *mmRTI* latency is significantly lower than *microRTI*, even for large 40-node networks (for both 10 and 50 interferer cases). We thus argue that given its better localization accuracy (*cf.* Section V), *mmRTI* is better suited than *microRTI* to localize both static and mobile users.

B. AoI Coverage Analysis

A major difference between *mmRTI* and *microRTI* is the signal coverage over the AoI. Whereas omnidirectional *microRTI* transmissions cover the entire AoI, the directional *mmRTI* coverage depends on the number of network nodes and the antenna beamwidths. While

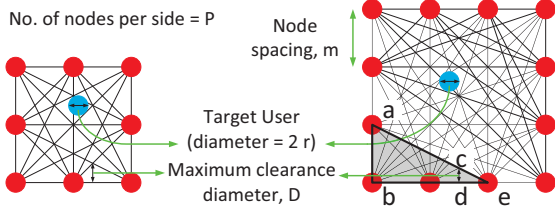


Fig. 4: Example directional sensing networks considered to determine the relation between the number of network nodes and the AoI size to ensure complete coverage.

complete signal coverage does not ensure accurate localization, it is essential to detect a user within the AoI. Accordingly, we present a study on the number of regularly-spaced directional nodes required to ensure complete *mmRTI* coverage of the AoI. For our study, we consider directional square networks, as shown in Fig. 4, with P nodes per side, with a spacing of q between them. For simplicity, we ignore the antenna beamwidths and consider the more stringent condition where the target user must cross the *line* connecting two nodes to be detected along the link. To determine the coverage condition, we derive the relationship between P , q , and the *maximum clearance diameter*, D , in the network. Fig. 4 shows that the maximum clearance in a network is near its edges, where only a few links cross through. For the example 12-node network shown in Fig. 4, we have $D = cd$ and $P = 4$. To determine the relation between P , q , and D , we consider $\triangle aeb$ and use the intercept theorem for parallel lines, which states that, for $ab \parallel cd$,

$$\frac{cd}{ab} = \frac{de}{be}. \quad (6)$$

For any square network with an even value¹ of P , be is equal to $(Pq)/2$. Additionally, given the network symmetry, de is equal to half the node spacing, or $q/2$. Hence, we derive the maximum clearance diameter,

$$D = cd = \frac{de}{be} \cdot ab = \frac{q/2}{(Pq)/2} \cdot q = \frac{q}{P}. \quad (7)$$

To determine the AoI coverage condition, we assume a cylindrical model for the target user (circular cross section radius, r), and that the target user is detectable within the AoI if at least one link cuts through it. For practical applications, we consider $r = 0.15$ m (average human body circumference is 1 m [17]). Complete AoI coverage is possible when the target user has at least the same diameter as the maximum clearance diameter (i.e., $D = 2r = 0.3$ m). Namely, using (7), a network with P nodes per side can completely cover an AoI of size $[(P-1)q]^2 = [0.3P(P-1)]^2$, where $q = 0.3P$. Accordingly, in Fig. 5, we present the upper bound relation between the number of nodes per side, the AoI size and the node spacing to ensure complete AoI coverage and the detectability of a target user of radius

¹The relation in (7) holds for odd values of P as well. We exclude the proof here for brevity.

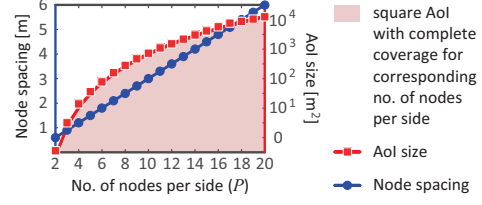


Fig. 5: Upper bound on the node spacing and the AoI size with respect to the number of nodes per side for a square network to ensure complete AoI coverage for detecting a human target.

$r = 0.15$ m. Fig. 5 shows that we need only 16 nodes to completely cover a standard room of size 10 m^2 , thereby demonstrating that *mmRTI* can cost-effectively detect people indoors.

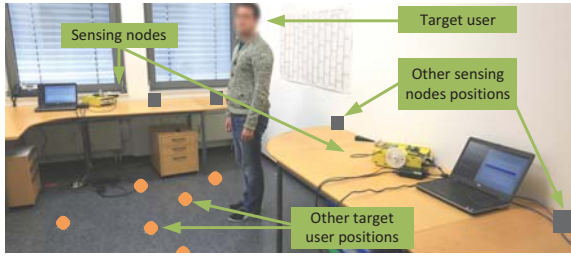
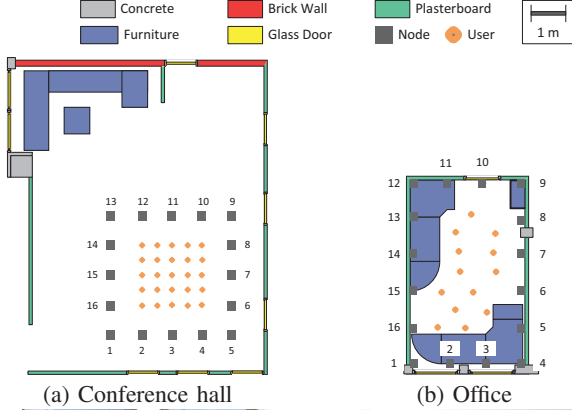
IV. EXPERIMENTAL EVALUATION

We experimentally evaluated the performance of *mmRTI* and *microRTI*, using sensing networks of highly-directional 60 GHz and omnidirectional 2.4 GHz nodes, respectively, under no external influence in two distinct indoor scenarios, and with human movement outside the AoI for one of the scenarios. For our experiments, we deployed sensing networks of sixteen nodes each. For each deployment, we obtained the instantaneous RSS measurements for different target user locations within the AoI, and estimated the target user locations by processing the RSS changes via the shadow RTI algorithm. In the following, we present the measurement scenarios, and the measurement hardware and procedures for the two sensing networks.

A. Measurement Scenarios

We deployed the sensing networks in two different locations: a clutter-free, large conference hall of size $9 \text{ m} \times 7 \text{ m}$, and a cluttered, small office of size $5 \text{ m} \times 3 \text{ m}$. Whereas in the conference hall², all nodes were placed with no furniture in the vicinity, in the office some nodes were placed on top of the tables. The deployment environments, the node positions, and the target user locations inside the AoI are shown in Fig. 6. We evaluated the performance of *mmRTI* and *microRTI* under near-ideal conditions in both the locations to investigate the effects of the different frequency bands and antenna types. Additionally, we studied the effects of external human motion in the conference hall, where such motion is realistically expected. For this experiment, the external motion effects are introduced by a single person walking randomly around and in close vicinity of the networks, without entering the AoI.

²Given the AoI symmetry in the conference hall, and assuming RSS reciprocity for a link between two nodes for a given target user location, we measured the RSS in the conference hall for transmissions from nodes 1-4 only for *mmRTI*. The RSS measurements for nodes 5-16 transmissions were then determined by rearranging the measurements for nodes 1-4 transmissions. This was done considering the significantly higher time required to measure RSS in *mmRTI* compared to *microRTI*, given our manual directional antenna steering measurement setup.



(c) Illustration of a target user in the AoI.

Fig. 6: Sensing network deployment locations and node positions for *mmRTI* and *microRTI* localization experiments.

B. Measurement Hardware and Procedures

For *mmRTI*, we employed the 60 GHz transceivers [18] in Fig. 7, where each node consists of a NI USRP SDR connected to a SiversIMA mm-wave up/down converter. The transceivers are controlled by host PCs running open-source *GNU Radio* code. For our measurements, the nodes are equipped with fixed, standard gain horn antennas with beamwidth of 10° and gain of 25 dBi, and transmit at a power of 0 dBm. Given our fixed antenna setup, we manually aligned antennas for a given 60 GHz node pair along their LOS orientations before measuring the RSS. To simplify the measurement process, we measured the RSS for one link at a time, i.e., only one node received when a node transmitted. While for our present implementation, we manually re-steer the antennas, we assume that for upcoming mm-wave nodes with on-chip beamforming antennas, re-steering will be done electronically using look-up tables with pre-determined LOS orientations for the node pairs.

For *microRTI*, we used the 2.4 GHz node in Fig. 8. As in [5], [6], each node comprised of a Raspberry Pi 3 single-board computer and a TP-Link TL-WN722N adapter, supporting IEEE 802.11 b/g/n PHYs in the 2.4 GHz band and featuring an omnidirectional antenna of 4 dBi gain. The 2.4 GHz nodes formed an independent basic service set, with each node assigned an IP address in the same subnet to ensure point-to-point communication. For the RSS measurements, we executed a *python* script on the nodes that automatically exchanged packets over links, such that each node broadcasted UDP

TABLE I: SENSING NETWORK & RTI PARAMETERS

Sensing network	<i>Node Spacing</i>	1.00 m
	<i>Node Height</i>	0.95 m
	<i>Transmit Power</i>	<i>microRTI</i> : 20 dBm (Ch. 1) <i>mmRTI</i> : 0 dBm
	<i>Antenna Gain</i>	<i>microRTI</i> : 4 dBi <i>mmRTI</i> : 25 dBi (10°)
RTI algorithm	<i>Pixel Size</i>	0.10 m
	<i>LOS Par., λ</i>	0.01 m
	<i>Regularization</i>	Tikhonov ($\alpha = 2$)

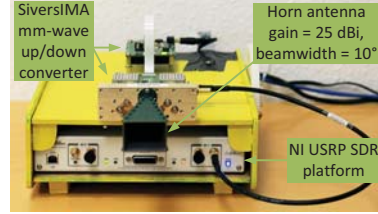


Fig. 7: 60 GHz sensing node, consisting of a USRP-SiversIMA transceiver with 10° beamwidth horn antenna.

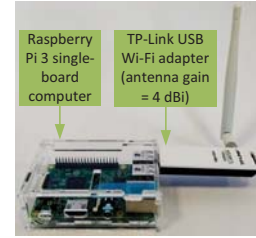


Fig. 8: 2.4 GHz sensing node, consisting of a Raspberry Pi 3 single-board computer with a TP-Link USB Wi-Fi adapter.

datagrams periodically to the IP addresses in the sensing network subnet on IEEE 802.11 channel 1 with a power of 20 dBm. The packet exchange timing is as per the CSMA/CA MAC scheme of Wi-Fi.

After the RSS is measured for all the sensing network links, the data is then forwarded to a central computer that computes the RSS changes with respect to the *empty-AoI* RSS values, and then processes them to generate the attenuation image via the shadow RTI algorithm in Section II. The used RTI algorithm and sensing network parameters are given in Table I.

V. PERFORMANCE ANALYSIS

In this section, we present and compare the localization performance of *mmRTI* and *microRTI*, with and without external human movement, based on the experiments described in Section IV.

A. Performance under Near-Ideal Conditions

In Fig. 9, we present the localization errors for *mmRTI* and *microRTI* for measurements under near-ideal conditions. The error distributions are obtained for all the target user locations in the AoI, as shown in Fig. 6. Fig. 9 shows that *microRTI* performs poorly in both scenarios compared to *mmRTI*. Whereas 90%-ile errors of 2.48 m and 2.85 m are obtained using *microRTI* in the conference hall and the office, respectively, *mmRTI*

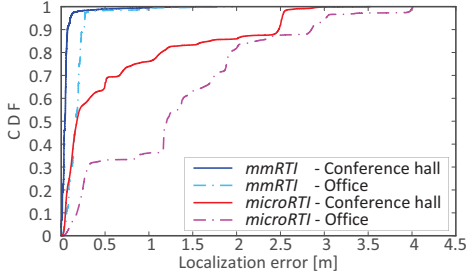


Fig. 9: Localization error for *mmRTI* and *microRTI* for sensing network deployments in a conference hall and an office (measurements under near-ideal conditions).

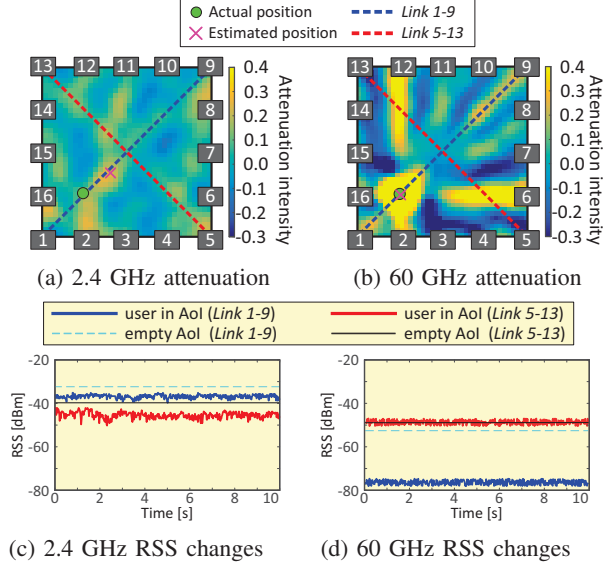


Fig. 10: Example attenuation images and RSS changes on two links (*Link 1-9*: user blocking LOS; *Link 5-13*: user not blocking LOS) for 2.4 GHz (*microRTI*) and the 60 GHz (*mmRTI*) sensing networks in near-ideal conditions.

achieves 90%-ile errors of 0.07 m and 0.25 m for the same scenarios. *mmRTI* locates a target user with an error below 1 m for 99% of the cases in both scenarios; by comparison, *microRTI* obtains an error below 1 m for only 76% and 36% cases, respectively. The poor performance of *microRTI* is primarily due to higher multipath propagation indoors for the omnidirectional, 2.4 GHz transmissions compared to the directional, 60 GHz transmissions in *mmRTI*. Accordingly, the 2.4 GHz network RSS changes are not exclusively dependent on the LOS link shadowing, thereby deviating from the underlying LOS-based RTI principle to estimate incorrect positions. These multipath effects are more dominant in smaller, more cluttered environments, as is evident by comparing the conference hall and the office results in Fig. 9. On the other hand, the 60 GHz network for *mmRTI* is largely isolated from the multipath effects due to its highly directional, LOS-dominant transmissions. Therefore, as *mmRTI* inherently adheres closely to the underlying RTI principles, we observe considerably better localization

accuracy. Nevertheless, *mmRTI* is not able to eliminate the multipath effects completely. Consequently, in Fig. 9, we observe slightly better *mmRTI* performance in the conference hall than in the office.

In Figs. 10a and 10b, we present the attenuation images for a user in the AoI to illustrate the multipath effects on the 2.4 GHz and the 60 GHz networks, respectively. We observe that the attenuation contrast is distinctly higher for the 60 GHz network, showing the dominant effects of the links whose LOS components are directly obstructed by the user, i.e., *Link 1-9* (between nodes 1 and 9), *Link 2-12* and *Link 6-16*. In Figs. 10c and 10d, we present the RSS drop for *Link 1-9* (link with the user in its LOS path) and *Link 5-13* (link with the user not in its LOS path). For the 60 GHz network, we observe that while *Link 1-9* experiences a large RSS drop due to the user shadowing the LOS component, there is nearly no RSS drop in *Link 5-13*. By contrast, the RSS drops for both links in the 2.4 GHz network are nearly equal. However, the 2.4 GHz link RSS drops are much smaller compared to the RSS drop in *Link 1-9* for the 60 GHz network. This illustrates that in the 2.4 GHz network: (a) there exist strong NLOS components of *Link 1-9*, as LOS shadowing by the user does not considerably reduce the link RSS, and (b) the user obstructs possible NLOS components of *Link 5-13* to cause the RSS drop.

B. Performance with External Human Movement

In Fig. 11, we present the localization results under the influence of human motion around the sensing network for *mmRTI* and *microRTI*. Fig. 11 shows that the localization accuracy is severely degraded for *microRTI* due to the external movement. Whereas *microRTI* estimates positions with an error of less than 1 m for 76% of the cases without human movement, the error is below 1 m for only 64% of the cases with human movement. By contrast, the estimation accuracy in *mmRTI* remains largely unaffected by human motion, as an error of less than 1 m is achieved for 99% of the cases under both conditions. The *microRTI* performance degrades for the 2.4 GHz network because such movements close to the network nodes create a non-stationary propagation environment that renders the mean, empty-AoI RSS values invalid. Consequently, the instantaneous RSS measurements fluctuate, even for a stationary target user, and thereby result in inaccurate localization. The 60 GHz nodes are largely isolated from such external motion, as the directional antennas limit the reception direction. Consequently, we observe robust localization accuracy for *mmRTI* with and without external human movement.

We can observe the effects of human movement that alter the signal propagation conditions from Fig. 12. The 2.4 GHz attenuation image in Fig. 12a shows a different attenuation distribution compared to the near-ideal condition image in Fig. 10a. However, comparing the

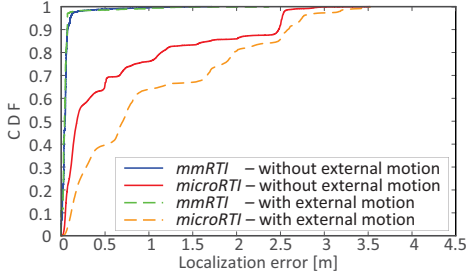


Fig. 11: Localization error for *mmRTI* and *microRTI* for sensing network deployment in the conference hall, with and without human movement around the sensing networks.

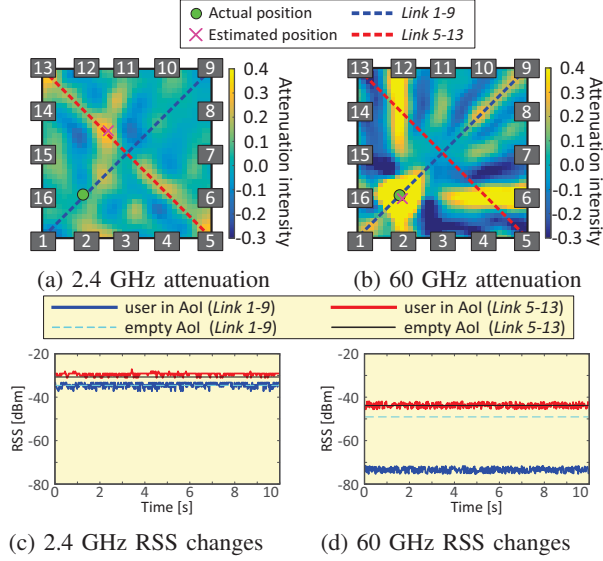


Fig. 12: Example attenuation images and RSS changes on two links (same links as in Fig. 10) for 2.4 GHz and the 60 GHz sensing networks with human movement around the networks.

60 GHz attenuation images in Figs. 10b and 12b, we observe no such difference. Furthermore, comparing Figs. 10d and 12d, we also observe that the RSS drops for the two links remain the same for the 60 GHz networks, regardless of human movement. By contrast, from Fig. 12c we see that the RSS drop is much smaller for *Link 1-9* compared to the RSS drop observed in Fig. 10c, indicating the reduced contribution of the LOS blockage on the RSS values; this is due to the new NLOS multipath components arising from the external motion.

VI. CONCLUSIONS

In this paper, we presented *mmRTI*, a novel, highly-directional, mm-wave sensing network based RTI approach, designed to overcome the effects of multipath and external human movement effects that severely degrade the indoor localization accuracy of the conventional *microRTI* approach. Our experimental evaluations in two distinct indoor scenarios revealed that, under near-ideal conditions, *mmRTI* achieved 90%-ile localization errors of 0.07 m and 0.25 m in the conference

hall and office environments, respectively. By contrast, *microRTI* obtained 90%-ile errors of 2.48 m and 2.85 m, respectively. Furthermore, we experimentally showed that *mmRTI* remained unaffected by external human movement, whereas the *microRTI* accuracy degraded by up to 1.2 m. Additionally, we argued that given the high access delay in CSMA/CA-based 2.4 GHz networks, the *mmRTI* measurement latency can be considerably lower than *microRTI*, thereby supporting effective localization of mobile targets. Therefore, given its robust and accurate localization capabilities, we argue that *mmRTI* is better suited for indoor localization in context-aware IoT applications.

REFERENCES

- [1] N. Patwari and P. Agrawal, "Effects of correlated shadowing: Connectivity, localization, and RF tomography," in *Proc. IPSN*, Apr. 2008, pp. 82–93.
- [2] C. Perera *et al.*, "Context aware computing for the Internet of Things: A survey," *IEEE Commun. Surveys Tuts.*, vol. 16, no. 1, pp. 414–454, May 2014.
- [3] A. Al-Fuqaha *et al.*, "Internet of Things: A survey on enabling technologies, protocols, and applications," *IEEE Commun. Surveys Tuts.*, vol. 17, no. 4, pp. 2347–2376, Jun. 2015.
- [4] J. Wilson and N. Patwari, "Radio tomographic imaging with wireless networks," *IEEE Trans. Mobile Comput.*, vol. 9, no. 5, pp. 621–632, May 2010.
- [5] A. Patra *et al.*, "Experimental evaluation of radio tomographic imaging algorithms for indoor localization with Wi-Fi," in *(accepted for) IEEE Globecom*, Dec. 2017.
- [6] S. Wittig, "Radio tomography using low-cost Wi-Fi devices," Master's thesis, iNETS, RWTH Aachen, Germany, 2016.
- [7] O. Kaltiokallio *et al.*, "Enhancing the accuracy of radio tomographic imaging using channel diversity," in *Proc. MASS*, Apr. 2012, pp. 254–262.
- [8] —, "A fade level-based spatial model for radio tomographic imaging," *IEEE Trans. Mobile Comput.*, vol. 13, no. 6, pp. 1159–1172, Jun. 2014.
- [9] J. Wilson and N. Patwari, "See-through walls: Motion tracking using variance-based radio tomography networks," *IEEE Trans. Mobile Comput.*, vol. 10, no. 5, pp. 612–621, May 2011.
- [10] F. Giannetti *et al.*, "Mobile and personal communications in the 60 GHz band: A survey," *Wirel. Pers. Commun.*, vol. 10, no. 2, pp. 207–243, Jul. 1999.
- [11] H. Yang *et al.*, "Indoor channel measurements and analysis in the frequency bands 2 GHz and 60 GHz," in *Proc. IEEE PIMRC*, vol. 1, Sep. 2005, pp. 579–583.
- [12] A. Molisch *et al.*, "Propagation channel models for next-generation wireless communications systems," *IEICE Trans. on Commun.*, vol. E97B, no. 10, pp. 2022–2034, Oct. 2014.
- [13] S. Singh *et al.*, "Interference analysis for highly directional 60 GHz mesh networks: The case for rethinking medium access control," *IEEE/ACM Trans. Netw.*, vol. 19, no. 5, pp. 1513–1527, Oct. 2011.
- [14] T. S. Rappaport *et al.*, "State of the art in 60 GHz integrated circuits and systems for wireless communications," *Proc. IEEE*, vol. 99, no. 8, pp. 1390–1436, Aug. 2011.
- [15] T. Sakurai *et al.*, "MAC access delay of IEEE 802.11 DCF," *IEEE Trans. Wireless Commun.*, vol. 6, no. 5, pp. 1702–1710, May 2007.
- [16] K. Chandra *et al.*, "Performance analysis of IEEE 802.11ad MAC protocol," *IEEE Commun. Lett.*, vol. PP, no. 99, pp. 1–1, 2017.
- [17] Body Measurements. Centers for Disease Control and Prevention. Last visited: 25-05-2017. [Online]. Available: <https://www.cdc.gov/nchs/fastats/body-measurements.htm>.
- [18] J. Arnold *et al.*, "Demo: Spectrum-agile mm-wave packet radio implementation on USRPs," in *Proc. ACM SRIF*, Sep. 2015, pp. 5–8.